N-S versus E-W extension in the Tibetan plateau: Are they driven by the same dynamics?

Giridas Maiti[1], Arnab Roy[2] and Nibir Mandal[2]

[1]Institute of Applied Geosciences,
Karlsruhe Institute for Technology, Germany

[2]Department of Geological Sciences, Jadavpur University
Kolkata 700032, India

N-S versus E-W extension in the Tibetan plateau: Are they driven by the same dynamics?

Giridas Maiti*[1], Arnab Roy[2], and Nibir Mandal[2]

[1] Institute of Applied Geosciences, Karlsruhe Institute for Technology, Germany
[2]Department of Geological Sciences, Jadavpur University, Kolkata, India

***Corresponding author:** Giridas Maiti (giridas.maiti@kit.edu)

Summary

The tectonic history of the Himalaya-Tibet Mountain Range records two important extensional tectonic events: 1) N-S extension in the Himalaya-Tibet transition zone, and 2) E-W extension in the southern and central Tibet, manifested in the form of east-west and north-south striking normal faults, respectively. The N-S extensional event (~22 Ma) started to commence earlier than the E-W extension (~18 Ma) and phased out by ~11 Ma, whereas the E-W extension continued to recent time (~4 Ma), suggesting a temporally overlapping period of ~7 Myr. This article addresses the question- did they originate from the same dynamical process? Using numerical and laboratory experiments, we show that a decreasing India-Asia convergence velocity induced gravitational collapse of the Tibetan plateau is the main driving force for both the extensional tectonic events, but they were controlled by two different mechanisms. Our results show that with a drop in the convergence velocity southern Tibet underwent gravitational collapse due to pressure relaxation in the underlying Himalayan wedge, and the collapse forced the deep crustal materials to extrude up, creating N-S extension (22 – 11 Ma) along the Himalaya-Tibet transition zone. On the other hand, presence of rigid Tarim block in north-western Tibet caused differential topographic uplifts from west to east, resulting in a first-order eastward topographic gradient of 0.1° during the initial fast-stage of India-Asia collision (> 22 Ma). Later on, this topographic slope prompted eastward crustal flows in the course of gravitational collapse, leading to E-W extensional tectonics (~18 - 4 Ma) in Tibet.

Keywords: India-Asia collision; Gravity collapse; Crustal flow velocity; Laboratory modelling; Strain-rate tensor

1. Introduction

Despite a prolong period of continuous India-Asia collision (~50 Ma), the present-day contractional deformations in the Himalaya-Tibetan orogen are primarily limited to its northern, northeastern and southern margins (Fig. 1a; Li *et al.* 2015, Zheng *et al.* 2017, Wang & Shen 2020), leaving a large portion of its interior region dominated by extensional tectonics. Two principal types of extensional structures are observed: 1) numerous N-S trending grabens and high-angle normal faults, located in the central Tibet, indicating E-W extensional deformation (Williams *et al*. 2001; Wang *et al*. 2014; Cooper *et al*. 2015) (Fig. 1b), and 2) E-W trending north-dipping, low-angle normal fault system, located at the Himalaya-Tibet transition zone, known as the South Tibetan Detachment System (STDS), indicating N-S extensional deformations (Fig. 1b). Geological data suggest that the N-S extensional tectonics (i.e., STDS) initiated at around 22 Ma and remained active to as late as 11 Ma (Fig. 1c; Kellett *et al.* 2009, 2013). The E-W extensional tectonics, on the other hand, initiated relatively at a later phase (ca. 18 Ma) of the India-Asia collision, and continued to operate till present-day, as warranted by a number of geological proxies, such as neo-tectonic faults (Armijo *et al.* 1986), offset quaternary deposits in the in the Ama Drime Massif and central Himalaya (Jessup *et al.* 2008), geophysical signatures, such as earthquake fault plane solutions (Andronicos *et al.* 2007) and GPS data (Zheng *et al.* 2017). Field investigations yield diverse temporal relations between N-S and E-W extensional structures; some suggesting E-W extension being younger than the N-S extension in some places (Hurtado *et al.* 2001, Murphy *et al.* 2002, Jessup *et al.* 2008, Hintersberger *et al.* 2010), whereas others showing more or less coeval occurrence (Mitsuishi *et al.* 2012). A compilation of the well constrained age data indicates that the two extensional events took place synchronously for at least 4 to 8 Ma during the early Miocene period (Fig. 1c; Cooper *et al.* 2015). This discussion leads us to the following stimulating question- did these orthogonally acting crustal extensions in Tibet originate from the same or different dynamics?

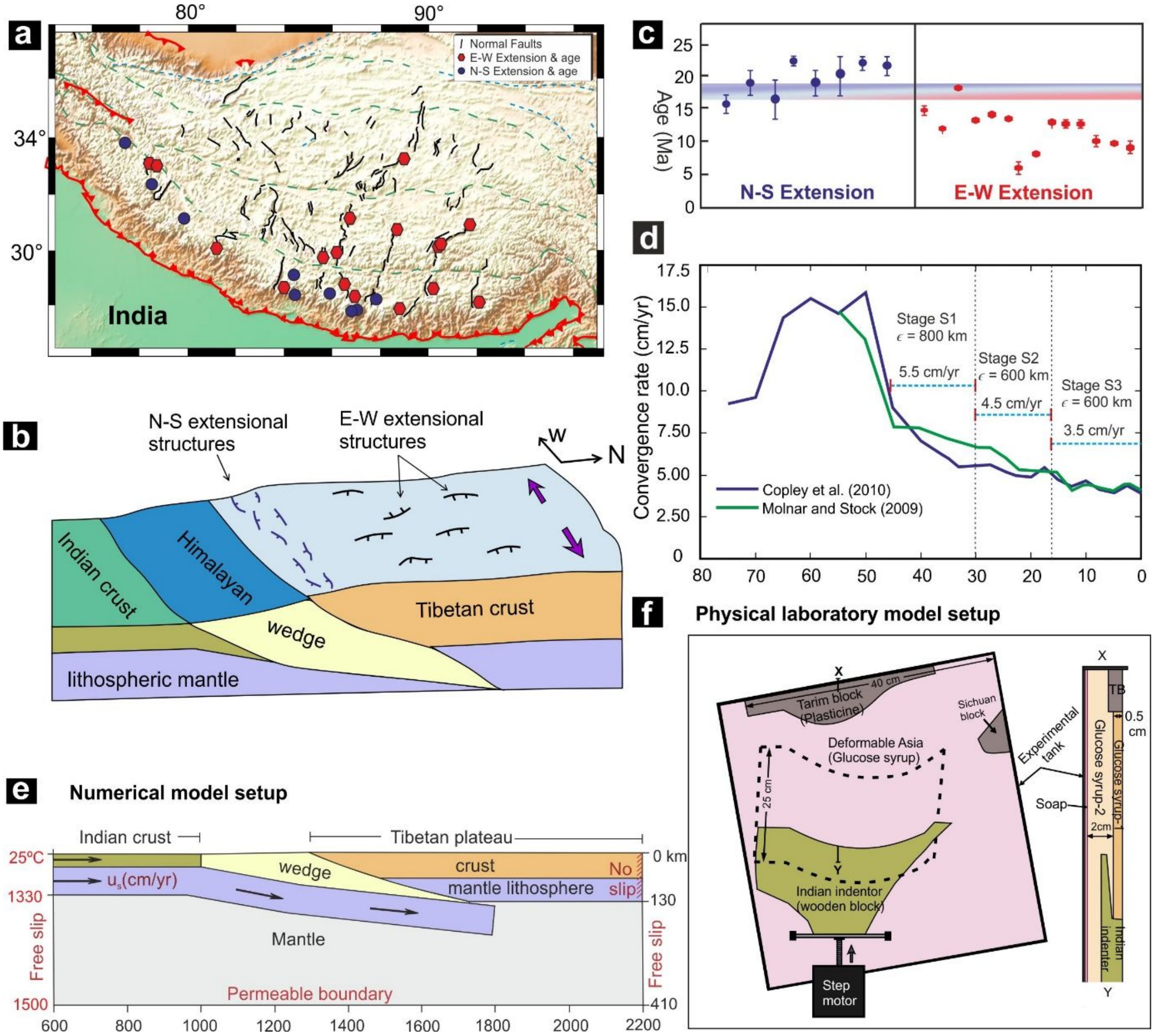

Figure 1: **a**) Spatial distribution of N-S and E-W extension related normal faults in the Himalaya-Tibetan plateau. **b**) Schematic 3D diagram of the Himalaya-Tibet orogeny showing spatial distribution of N-S and E-W extension related normal faults. **c**) Age distribution of N-S and E-W extensional faults which shows that N-S extensional faults are older than E-W extensional faults and they form ~7 Ma temporally overlapping period. **d**) Temporally decreasing India-Asia convergence velocity graph. Varying average indentation velocities for specific time intervals, considered in the laboratory models have been also indicated on the graph. **e**) 2D numerical model setup with thermal and kinematic boundary conditions used for numerical experiments. **f**) A schematic diagram of the top view of the laboratory model setup of India-Asia indentation experiment.

A number of tectonic models has been proposed to explain the initiation of E-W and N-S extensions during the India-Asia convergence. Existing N-S extensional models show the crustal extension at the southern margin of Tibet as a consequence of either the southward extrusion of deep crustal metamorphic core in the Higher Himalaya (Beaumont *et al.* 2001, Grujic *et al.* 2002, Maiti & Mandal 2021) or formation of passive roof structure above a contractional wedge in the Himalaya (Kohn 2008). The driving mechanism for E-W extension, on the other hand, is a debated subject, despite a remarkable advancement in Tibetan tectonic modelling over the last few decades, which include convective removal of mantle lithosphere (England & Houseman 1989), lateral extrusion of crustal materials (Tapponnier *et al.* 1982, Hintersberger *et al.* 2010, Mitsuishi *et al.* 2012), lower crustal flow (Pang *et al.* 2018), oblique convergence (McCaffrey & Nabelek 1998), and far field extensional forces (Schellart *et al.* 2019). The work of Copley & Mckenzie (2007) suggested that currently southern and eastern part of Tibetan plateau are undergoing topography-driven gravity flow, and developing normal faults in the southern Tibet. However, most of these earlier models treated the dynamics of two extensional tectonics (i.e., N-S and E-W) separately, giving no dynamic connections between the two tectonic processes. Moreover, it is yet to resolve the questions- what caused their long overlapping period of extensional activities (7 to 8 Ma) and why the N-S extensional event eventually seized by ~11 Ma, allowing the E-W extension to remain active till present day. From numerical and scaled laboratory models this study addresses the problem of dynamic connection between the E-W and N-S crustal extensions in the Himalaya-Tibet system. It is demonstrated that they originated from two distinctly different parallel tectonic processes, where the reducing India-Asia convergence rate has acted as the unifying kinematic factor to govern them.

2. Methods and model setup

Tectonic reconstruction studies suggest India-Asia collision occurred with decreasing convergence rates from ~15 cm/yr at 50 Ma to ~3.5 cm/yr at the present-day (Molnar & Stock 2009, Copley *et al.* 2010). Using thermo-mechanical numerical and scaled laboratory experiments we investigate whether such a retarding Indian indentation could be the main factor in driving both the N-S and E-W extensional tectonics in the Himalaya-Tibet. In the numerical experiments, we modelled the Himalayan wedge with low-viscosity (μ) and -density (ρ) crustal materials ($\mu = \sim 10^{20}$ -10^{21} Pa s; ρ = 2600–3050 kg/m^3), sandwiched between the relatively stronger colliding Indian plate ($\mu = \sim 10^{21}$ -10^{23} Pa s; ρ = 2750–3250 kg/m^3) and the overriding Tibetan plateau (Fig. 1e). Our thermomechanical modelling implements the conservation equations for mass, momentum and energy as follows.

$$\rho \nabla . \boldsymbol{u} = 0, \quad (1)$$

$$-\mu \nabla^2 \boldsymbol{u} + \nabla p = \boldsymbol{F}, \quad (2)$$

$$\rho C_p \frac{\partial T}{\partial t} + \rho C_p \boldsymbol{u} \cdot \nabla T = \nabla \cdot (k \nabla T) + Q_{sh}, \quad (3)$$

where $\boldsymbol{u}$, μ, ρ, p, $\boldsymbol{F}$, denote velocity vector, viscosity, density, pressure, and body force term, respectively. In Equation (3), the thermodynamic parameters T, Cp, k, Q_{sh} represent temperature, specific heat, thermal conductivity, and heat source respectively. The values of different parameters and material properties chosen in our models are listed in Supplementary Table S1.

To model the 3D topographic evolution and associated crustal flows in the Himalaya-Tibet orogeny, we develop an indentation model, replicating the decreasing India-Asia collision velocity in a 3D scaled-laboratory setup within a framework of thin viscous sheet (TVS) approximation (England & McKenzie 1982, Yang & Liu 2013, Maiti *et al.* 2021). The continental lithosphere is usually modelled with viscous rheology to represent its large-scale and long-term deformation behaviour (Ellis 1996, Copley & Mckenzie 2007). Similarly, we have used appropriately scaled analogue viscous materials to model crustal-lithosphere and

127 underlying sub-crustal mantle region of the Tibetan plateau. The top 40 km thick crustal-
128 lithosphere is modelled using glucose syrup-1 (ρ_{cl} = 1406 ± 3 kg/m^3, μ_{cl} = 305 ± 5 Pa s), which
129 represents a depth-averaged physical properties of the corresponding natural prototype (density:
130 2,780 kg/m^3, viscosity: 3 × 10^{21} Pa s). Glucose syrup-2 (μ_{sm} = 28 ± 5 Pa s; ρ_{sm} = 1,510 ± 5
131 kg/m^3) has been used to model the underlying sub-crustal mantle region (viscosity: ∼10^{20} Pa
132 s; density: 3,200 kg/m^3) (Jiménez-Munt *et al*. 2008). We have chosen commercial plasticine
133 mixed with oil (viscosity = 3 × 10^5 Pa s; density = 1.5 gm/cc) (Zulauf & Zulauf 2004) to
134 represent relatively strong Tarim and Sichuan blocks. The wooden indenter plate in our model
135 setup mechanically replicates a relatively much stronger colliding Indian plate. The
136 experimental setup consists of a 40 ×50 cm rectangular box with a depth of 3 cm (Fig. 1f). The
137 width 40 cm in the model represents approximately 3200 km east-west length of the Tibetan
138 plateau. This gives rise to nature to model length ratio 1.25 × 10^{-7}. The properties of analogue
139 materials and model scaling ratios are provided in Supplementary Table S2. We gradually
140 reduced the indentation velocity from an initial average of 5.5 cm/yr to present-day 3.5 cm/yr,
141 in accordance with the convergence velocity-time regression (Fig. 1d). The initial position of
142 Indian indenter's leading-edge is kept at a distance, scaled to 2000 km south from the present-
143 day position (Schellart *et al.* 2019). The shortening of this distance is attained in three
144 successive stages: S1, S2, and S3 with shortening (ϵ) of 800, 600, and 600 km, and 5.5, 4.5,
145 and 3.5 cm/yr, respectively. For a quantitative analysis of the model crustal-flow velocity, we
146 use a particle image velocimetry system, called PIVLab (details in Supplementary-S2).
147

148 **3. Results**

149 *3.1. N-S extension in 2D numerical models*

150 Our 2D thermomechanical numerical model results suggest during the early phase of
151 fast India-Asia collision the downgoing motion of the subducting Indian plate (subduction

velocity, u_s = 8 cm/yr) produced a high lubrication dynamic pressure in the Himalayan wedge (Maiti & Mandal 2021) and facilitated burial of buoyant crustal rocks into the wedge (Fig. 2a). This dynamic state was able to transfer large amount of contractional stress to the overriding Tibetan lithosphere and developed higher topographic upliftment (Fig. 2a). The magnitudes of lubrication dynamic pressure started to drop with reducing subduction velocity (Fig. 2c), and the collision system eventually attained a threshold condition when u_s dropped below 5 cm/yr. Under this critical state of low dynamic pressure, the Himalayan wedge failed to transmit sufficient contractional stress to support the elevated topography of the overriding Tibetan lithosphere produced in the fast collision phase, and resulted in gravitational collapse in the uplifted and thickened Tibetan crust (Fig. 2b). The collapse of the Tibetan plateau started to occur preferentially at the southern margin of Tibet, which forced the deep-crustal materials in the Himalayan wedge to extrude in the form of a spontaneously developed extrusion channel, bounded by two oppositely directed shear zones with a normal sense of shear on the top and a thrust sense of shear at the bottom (Fig. 2b). The normal sense of shear in the model is located close to the Himalaya-Tibet suture zone, and represents the N-S extensional tectonics, as manifested in the form of STDS fault systems at the southern margin of Tibet (Fig. 2b-ii; Carosi *et al.* 2018). The thrust sense of shearing at the bottom of extrusion channel indicates concurrently occurring contractional tectonics in the Himalayan wedge, recorded in the Main Central Thrust (MCT) (Carosi *et al.* 2018, Maiti & Mandal 2021). Continued gravity collapse of the overriding Tibetan lithosphere upon the Himalayan wedge eventually raised the dynamic pressure and equilibrated the system (Maiti & Mandal 2021). This transformation led to cessation of STDS faulting, i.e. N-S extensional tectonics in the Himalaya-Tibet transition zone. However, our 2D numerical model evidently cannot explain the deformation dynamics in the east-west direction. We therefore conduct 3D laboratory experiments to interpret the E-W extensional tectonics, which is discussed below.

177

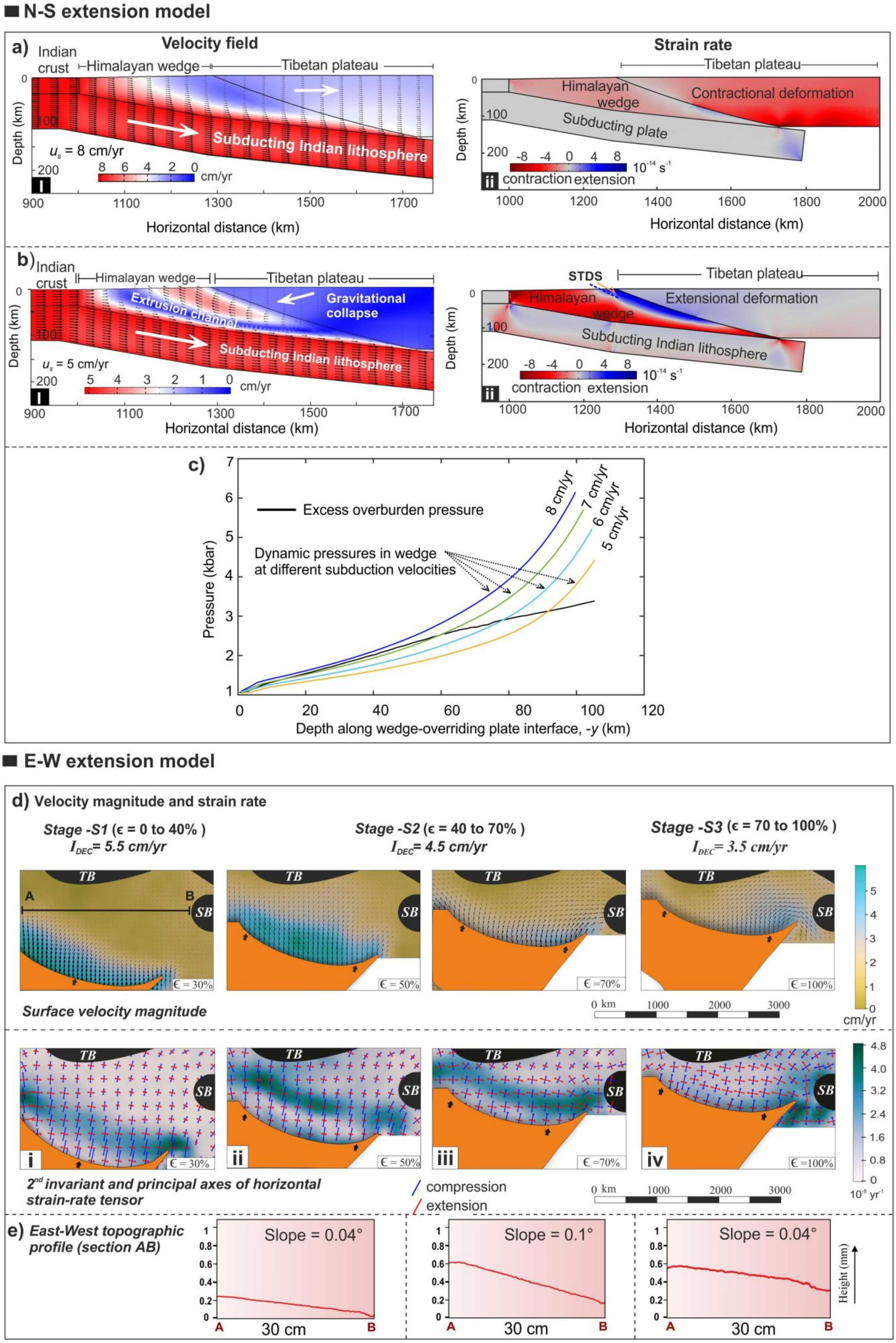
N-S extension model
a) Velocity field
Indian crust
Himalayan wedge
Tibetan plateau
Subducting Indian lithosphere
u_s = 8 cm/yr
cm/yr
Depth (km)
Horizontal distance (km)
Strain rate
Himalayan wedge
Contractional deformation
Subducting plate
contraction extension
10^{-14} s^{-1}
b) Indian crust
Extrusion channel
Gravitational collapse
u_s = 5 cm/yr
STDS
Extensional deformation
c) Excess overburden pressure
Dynamic pressures in wedge at different subduction velocities
8 cm/yr
7 cm/yr
6 cm/yr
5 cm/yr
Pressure (kbar)
Depth along wedge-overriding plate interface, -y (km)
E-W extension model
d) Velocity magnitude and strain rate
Stage -S1 (ϵ = 0 to 40%) I_{DEC}= 5.5 cm/yr
Stage -S2 (ϵ = 40 to 70%) I_{DEC}= 4.5 cm/yr
Stage -S3 (ϵ = 70 to 100%) I_{DEC}= 3.5 cm/yr
TB
SB
Surface velocity magnitude
cm/yr
2nd invariant and principal axes of horizontal strain-rate tensor
compression
extension
10^{-8} yr^{-1}
e) East-West topographic profile (section AB)
Slope = 0.04°
Slope = 0.1°
Slope = 0.04°
30 cm
Height (mm)

Figure 2. **a**) and **b**) show plots of (i) velocity vectors and (ii) horizontal strain rates (ε_{xx}) in 2D numerical model at high subduction velocity, u_s = 8 cm/yr and threshold u_s = 5 cm/yr of the downgoing Indian plate. Note that the overriding Tibetan lithosphere is undergoing contractional deformation at u_s = 8 cm/yr, but at u_s = 5 cm/yr the Tibetan plateau undergoes extensional deformation due to gravitational collapse of the Tibetan plateau onto the Himalayan wedge. **c**) Calculated plots of dynamic pressure (P_{dy}) in the Himalayan wedge from analytical solution of lubrication dynamics (Maiti and Mandal, 2020) against excess overburden load (P_{ob}) acting onto the wedge-overriding plate interface. P_{ob} arises from topographic load and density difference between buoyant wedge rocks and denser overriding plate materials. Note that at u_s = 5 cm/yr the P_{dy} significantly dropped below the P_{ob}. **d**) Top views of 3D laboratory model run with decreasing indentation velocity (I_{DEC}) from 5.5 to 3.5 cm/yr. i) to iv) show snapshots of the crustal flow patterns taken at different percentage of the convergence (ϵ) and changes in the principal axes of horizontal strain-rate tensor (blue is compression, red is extension). **e**) N-S and E-W topographic profiles along AB and CD sections at different ϵ.

3.2. E-W extension in 3D laboratory models

Our 3D laboratory model accounts for the effects of lateral crustal heterogeneity in the form of Tarim and Sichuan basins to investigate exclusively the dynamics of eastward crustal flows and E-W extensional tectonics in Tibet under reducing India-Asia collision rates. In stage S1 (ϵ = 0 to 40%) (fast collision with an average indentation velocity of the Indian plate: U_{IND} = 5.5 cm/yr), the collision produced a strongly heterogeneous NNE-directed crustal-flow velocity, with negligibly small E-W velocity components (Fig. 2d-i). The northward flows localize in southern Tibet at high velocities (~5 cm/yr), but rapidly reduce northward, leaving the northern boundary of Tibet virtually unaffected. The strain maps, calculated from the model velocity fields in Stage-S1 show mainly N-S contractional deformations at a rate of 2×10^{-8} yr^{-1} in southern Tibet (Fig. 2d-i). The western region gained slightly higher topographic elevation relative to its eastern counterpart forming a gentle slope (0.04°) in the E-W direction (Fig. 2e).

In Stage S2 (ϵ = 40 to 70%; U_{IND} = 4.5 cm/yr), the NNE-directed high crustal velocity (~ 4.2 cm/yr) field propagated northward with crustal flows at the rates of ~1 cm/yr. At this stage the strong Tarim basin at the northern margin acted as a mechanical barrier to redirect the northward flows in north-east directions through the central and eastern Tibet (Fig. 2d-ii). In addition, the presence of this basin significantly constrained the effective width of western

Tibet to accommodate horizontal contraction, as compared to the much wider eastern flank of Tibet. Towards the end of Stage-S2 (ϵ = 70%), the model developed a plateau with steep topographic slopes (0.1º) in the east direction (Fig. 2e-ii). At this stage, measured contractional deformations across north to central Tibet is 2.5×10^{-8} yr^{-1} (Fig. 2d-ii).

In stage S3 (ϵ = 70 to 100%; U_{IND} = 3.5 cm/yr) of collision, the model showed a remarkable change in the crustal-flow pattern (Fig. 2d-iii). In southern Tibet, the flows occurred in the NNE direction with an average magnitude of 3.2 cm/yr, which decreased to ~2 cm/yr in northeastern Tibet, where they had a grossly ENE trend. The model developed a distinct region of east directed crustal-flows at the rates of 1.5 to 2 cm/yr in the central and eastern parts of the plateau (Fig. 2d-iii). The combined effects of eastward topographic gradient and gravitational collapse of the elevated plateau forced crustal materials to flow from western and central Tibet to the southeastern and northeastern regions.

The Stage-S2 to S3 transition is marked by initiation of E-W extensional strains (2×10^{-8} yr^{-1}), dominantly in the central and eastern Tibet (Fig. 2d-iii). In Stage-S3, the northern plateau margin continues to undergo horizontal contraction (1×10^{-8} yr^{-1}) (Fig. 2d-iii). The strain map for the present-day model configuration shows that the E-W extension eventually captures the entire Tibetan tectonics, leaving a small region of high contractional rates (4×10^{-8} yr^{-1}) between the eastern syntaxis and Sichuan basin. The strain distribution in the eastern flank of model Tibet is found to be strongly heterogeneous. On immediate south of this contraction region lies an extensional field of high strain rates (3×10^{-8} yr^{-1}; Fig. 2d-iii), which is a consequence of the flow divergence (fan like front in the Burma plate) in the extreme southeastern margin (Fig. 2d-iii, iv). At the end of stage S3 (ϵ =100%), the model produces an overall crustal-flow pattern (Fig. 2d-iv), very similar to the present-day GPS velocities measured in the Tibetan region (Zhang *et al.* 2004, Liang *et al.* 2013). Southern Tibet show NE-direction crustal flows, gradually changing to nearly east in the northeastern flank of Tibet, and eventually taking a clockwise turn between Eastern Himalayan Syntaxis (EHS) and Sichuan basin to escape in the south-east direction (~2.5 cm/yr), forming a fan-like front (Fig. 2d-iv). The gravitational collapse reduces the topographic gradient along the E-W (0.04º) direction (Fig. 2e-iii).

3.3. A unified 3D numerical model

To investigate whether the N-S and E-W extensional tectonics were driven by the same gravitational collapse dynamics, we developed a unified 3D numerical model using the same set of governing equations (Supplementary S3), as in our 2D model. Here we considered a subduction velocity of 4 cm/yr and an E-W topographic slope of 0.1º, as estimated from our 3D laboratory models at the end of Stage-S2 (Figs. 2e-ii, 3a). This initial model condition represented the ~22-18 Ma tectonic setting in the history of India-Asia collision. The model produces synchronously operating N-S extension in the Himalaya-Tibet transition zone and E-W extension in the central Tibet (Fig. 3b).

4. Discussion and conclusion

Our combined numerical and analogue modelling approach integrates the following crucial issues within a single geodynamic framework: 1) the underlying dynamics of N-S and E-W crustal extensions in Tibet, 2) the role of temporally retarding India-Asia collision in the extensional tectonics, and 2) the influence of rigid crustal blocks, such as Tarim and Sichuan basins in the evolution of 3D Tibetan topography with eastward topographic slopes that set in the present-day eastward crustal flows in the Tibetan plateau. The 2D numerical model suggests that the Himalayan wedge dynamics entirely controlled the N-S extension in the Himalaya-Tibet system, where the retarding India-Asia convergence kinematics played a mediated role, as explained in the following. According to the lubrication model, the downward movement of subducting Indian plate at a high velocity produced a large dynamic pressure in the wedge (Maiti *et al.* 2020, Maiti & Mandal 2021), which enabled the wedge to support the overriding

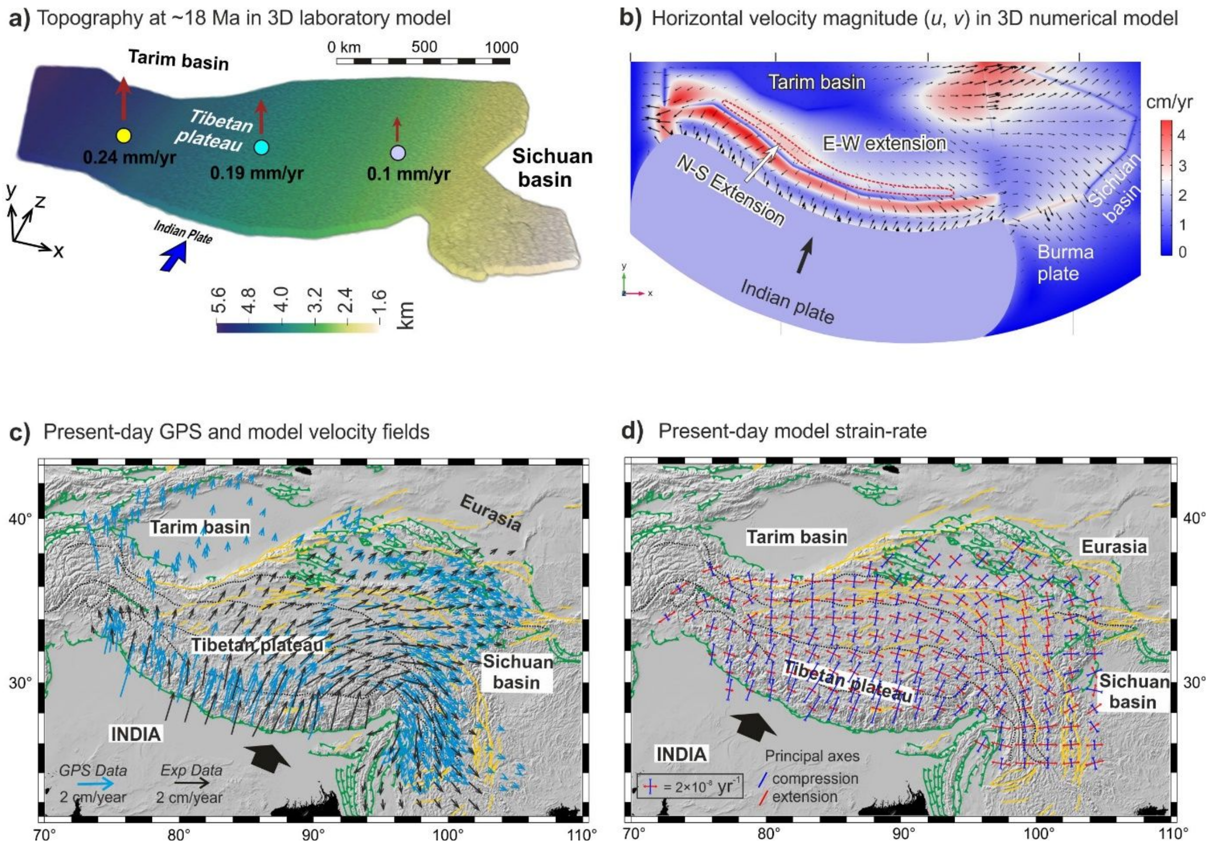

Figure 3. **a**) 3D topography in the laboratory model produced after 70% of total convergence. Note that there were different rates (average) of topographic uplift from west to east in the Tibetan plateau which gave rise to west to east topographic gradient. This topographic gradient was used in the 3D numerical model shown in panel-b. **b**) Calculated plots of velocity magnitudes in 3D numerical model at the moment of gravitational collapse (at ~ 18 Ma and u_s = 4.5 cm/yr). Comparison of the **c**) present-day GPS velocity field with model produced velocity, and **d**) present-day principal axes of horizontal strain-rate tensor (blue is compression, red is extension), derived from GPS velocities (after Zhang et al., 2004) and model results.

lithospheric load and at the same time transferred compressive stresses into the overriding Tibet. With decreasing plate velocity the dynamic pressure started to decline, as predicted from the lubrication mechanics (Fig. 2c; Maiti *et al.* 2020) and became sufficiently low so that the wedge failed to support the elevated Tibetan topography and initiated gravitational collapse at the southern margin of Tibet. The gravitational collapse, in turn, forced the deep-crustal materials in the Himalayan wedge to extrude in the southward direction that developed a N-S extensional tectonic setting in the form of STDS (Fig. 2b-ii). This N-S extension in the southern margin of Tibet was the first response to the reducing collision rate, the effect of which had some time lag (~3-4 Myr) to influence the differentially uplifted western and eastern Tibetan topography and to initiate the eastward crustal flows.

Our 3D laboratory model results suggest that the lateral crustal heterogeneities, Tarim and Sichuan basins critically controlled the evolution of the first-order eastward sloping plateau topography (0.1°), which later collapsed to set the eastward flows and developed E-W extension in the central Tibet as the indentation velocity reduced to the present-day level (3.5 cm/yr in average). Up-scaling of the model velocity field reveals that the mechanically strong Tarim basin in north acted as a mechanical obstruction to reduce the horizontal crustal-flow velocity, and facilitated the western and central Tibetan topography to uplift at faster rates (1.1 mm/yr), compared to the adjoining eastern and northeastern regions (0.5 mm/yr). This differential uplift gave rise to an eastward topographic slope in the period (~45 to ~18 Ma) of fast collision ($U_{IND} \geq 4.5$ cm/yr) (Fig. 2d). As U_{IND} decreased to 3.5 cm/yr at ~18 Ma, the topography collapsed with an eastward crustal-flow in the central plateau and gave rise to E-W extensional tectonics. The eastward flow eventually encountered the Sichuan basin in eastern Tibet and turned clockwise around the Eastern Himalayan Syntaxis (EHS) (Figs. 2d-III, IV). The present-day velocity magnitudes and their directions in the southern (~3.5 cm/yr), central (~3.2 cm/yr) and north-eastern Tibet (0.5 to 1 cm/yr) (Fig. 3c), as estimated in our study are consistent with the GPS data of ~4 cm/yr, ~3.5 cm/yr, and 0.5 to 1.5 cm/yr, respectively (Zhang *et al.* 2004, Gan *et al.* 2007, Liang *et al.* 2013). The model estimate of extensional strain rate in the central and southern Tibet is $0.8\text{-}2.2\times10^{-8}$ yr^{-1} (Fig. 3d), which also matches with the geodetic estimates (8 to 12×10^{-9} yr^{-1}, Ge *et al.* 2015). An overall agreement of the model-derived present-day crustal velocities and strain rates with the GPS data validate our model findings.

To summarize, this study substantiates the topography induced gravitational collapse theory for the Tibetan plateau to explain the extensional crustal deformations in the Himalaya-

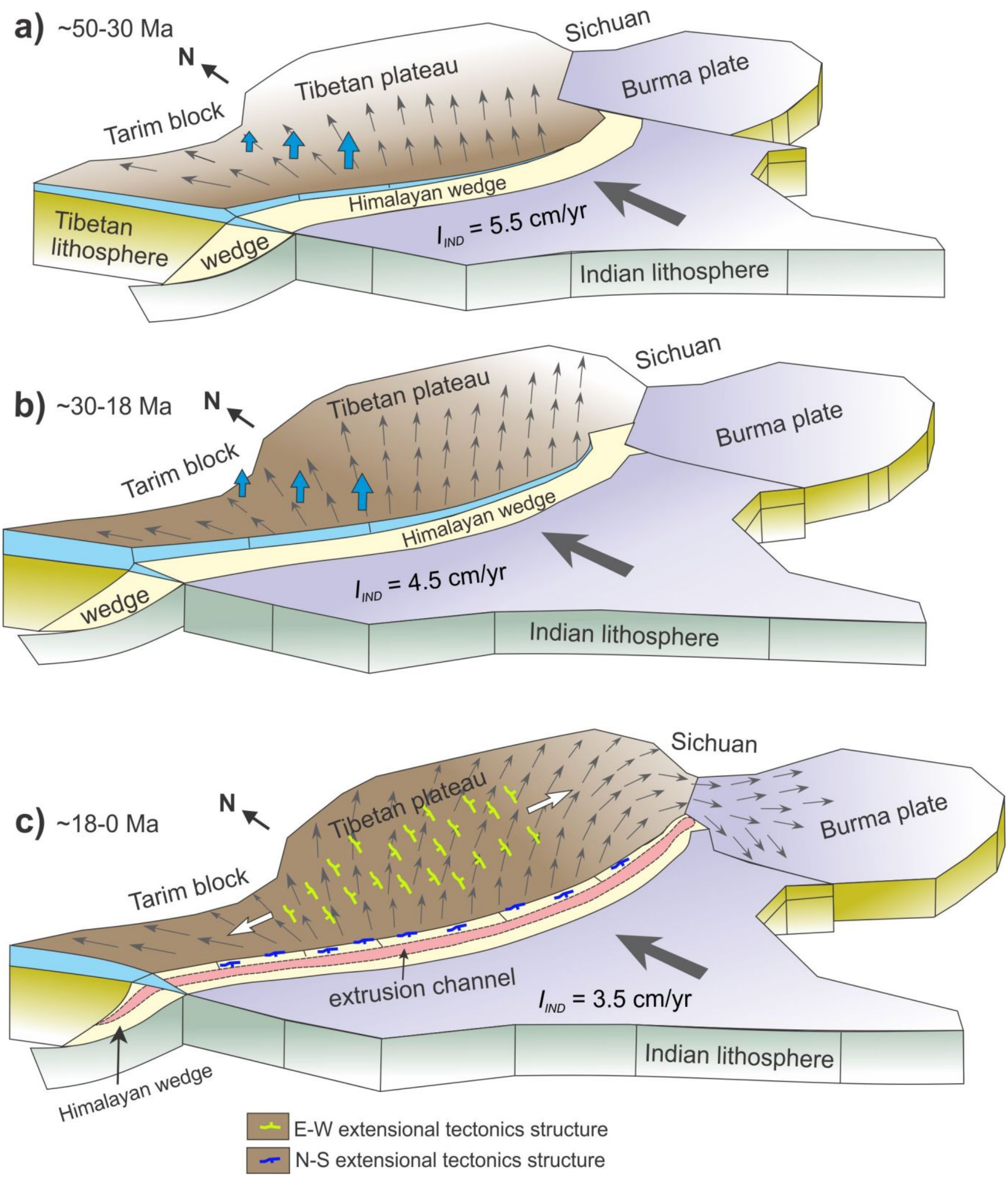

Figure 4. **a**) A schematic presentation of the deformation pattern in the Tibetan plateau with decreasing Indian indentation velocities (I_{IND}). (a) During high I_{IND} = 5.5 cm/yr, the collision produced an overall NNE-directed crustal flow in Tibet. b) With continuous northward indentation (I_{IND} = 4.5 cm/yr), crustal flows encountered resistance from rigid Tarim basin and were deflected towards northeast. At this stage the western and central Tibet uplifted at relatively higher rates, compared to eastern Tibet, creating an eastward topographic gradient

(0.1°). c) At 19 ± 3 Ma (ϵ = 70%), decrease of I_{IND} to the present average (3.5 cm/yr), resulted in gravitational collapse of the plateau, and initiated both N-S and E-W extensional tectonics.

Tibet system (Copley & Mckenzie 2007, Cook & Royden 2008). However, we argue that a coupled dynamics is required to explain the extension across and along the orogen, i.e. N-S and E-W, respectively. It is the drop in dynamic pressure in the Himalayan wedge that dictated the N-S extension in southern Tibet, whereas the topography-driven gravity current developed due to the eastward topographic gradient set in the E-W extension in central Tibet. However, the two tectonic events did not occur exactly in the same time frame; the N-S extension (22 – 11 Ma) ceased to operate as the dynamic pressure regained its initial state with ongoing topographic collapse, but the E-W extension (18-4 Ma) continued to take place in response to the eastward topographic slope under the present-day convergence kinematics. Therefore, we suggest reducing Indian plate's indentation velocity actually controlled the coupled extensional dynamics. Far-field tectonic stresses or convective instability might have provided additional influences on extensional tectonics (Schellart *et al.* 2019). But, a complete synthesis of our model results point to that a combined effect of the crustal heterogeneity and the reducing Indian indentation velocity is necessary and sufficient to explain the E-W extension.

Author contribution statement

GM and NM conceived the idea, GM wrote the manuscript, GM and AR conducted laboratory experiments, and AR analysed the data. This work is a part of the PhD thesis of GM and supported by the DST-SERB through J. C. Bose fellowship (SR/S2/JCB-36/2012) to NM. GM acknowledges support from the Karlsruhe Institute of Technology (KIT), Germany for hosting him as a postdoctoral researcher.

Data Availability Statement

The authors confirm that all the data supporting the findings of this study are available within the article. The GPS data used for comparison of model results are available in Zhang et al. (2004), Gan et al. (2007), and Zheng et al. (2017).

References:

Andronicos, C.L., Velasco, A.A. & Hurtado, J.M. (2007) Large-scale deformation in the India-Asia collision constrained by earthquakes and topography. *Terra Nov.*, **19**, 105–119, John Wiley & Sons, Ltd. doi:10.1111/J.1365-3121.2006.00714.X

Armijo, R., Tapponnier, P., Mercier, J.L. & Han, T.-L. (1986) Quaternary extension in southern Tibet: Field observations and tectonic implications. *J. Geophys. Res. Solid Earth*, **91**, 13803–13872, John Wiley & Sons, Ltd. doi:10.1029/JB091IB14P13803

Beaumont, C., Jamieson, R.A., Nguyen, M.H. & Lee, B. (2001) Himalayan tectonics explained by extrusion of a low-viscosity crustal channel coupled to focused surface denudation. *Nature*. doi:10.1038/414738a

Carosi, R., Montomoli, C. & Iaccarino, S. (2018) 20 years of geological mapping of the metamorphic core across Central and Eastern Himalayas. *Earth-Science Rev.*, **177**, 124–138, Elsevier. doi:10.1016/J.EARSCIREV.2017.11.006

Cook, K.L. & Royden, L.H. (2008) The role of crustal strength variations in shaping orogenic plateaus, with application to Tibet. *J. Geophys. Res. Solid Earth*. doi:10.1029/2007JB005457

Cooper, F.J., Hodges, K. V., Parrish, R.R., Roberts, N.M.W. & Horstwood, M.S.A. (2015) Synchronous N-S and E-W extension at the Tibet-to-Himalaya transition in NW Bhutan. *Tectonics*. doi:10.1002/2014TC003712

Copley, A., Avouac, J.P. & Royer, J.Y. (2010) India-Asia collision and the Cenozoic slowdown of the Indian plate: Implications for the forces driving plate motions. *J. Geophys. Res. Solid Earth*. doi:10.1029/2009JB006634

Copley, A. & Mckenzie, D. (2007) Models of crustal flow in the India-Asia collision zone. *Geophys. J. Int.* doi:10.1111/j.1365-246X.2007.03343.x

Ellis, S. (1996) Forces driving continental collision: Reconciling indentation and mantle subduction tectonics. *Geology*. doi:10.1130/0091-7613(1996)024<0699:FDCCRI>2.3.CO;2

England, P. & Houseman, G. (1989) Extension during continental convergence, with application to the Tibetan Plateau. *J. Geophys. Res.* doi:10.1029/jb094ib12p17561

England, Philip & McKenzie, D. (1982) A thin viscous sheet model for continental deformation. *Geophys. J. R. Astron. Soc.* doi:10.1111/j.1365-246X.1982.tb04969.x

Gan, W., Zhang, P., Shen, Z.K., Niu, Z., Wang, M., Wan, Y., Zhou, D., *et al.* (2007) Present-day crustal motion within the Tibetan Plateau inferred from GPS measurements. *J. Geophys. Res. Solid Earth*. doi:10.1029/2005JB004120

Ge, W.P., Molnar, P., Shen, Z.K. & Li, Q. (2015) Present-day crustal thinning in the southern and northern Tibetan Plateau revealed by GPS measurements. *Geophys. Res. Lett.* doi:10.1002/2015GL064347

Grujic, D., Hollister, L.S. & Parrish, R.R. (2002) Himalayan metamorphic sequence as an orogenic channel: insight from Bhutan. *Earth Planet. Sci. Lett.*, **198**, 177–191, Elsevier. doi:10.1016/S0012-821X(02)00482-X

Hintersberger, E., Thiede, R.C., Strecker, M.R. & Hacker, B.R. (2010) East-west extension in the NW Indian Himalaya. *GSA Bull.*, **122**, 1499–1515, GeoScienceWorld.

doi:10.1130/B26589.1

Hurtado, J.M., Hodges, K. V & Whipple, K.X. (2001) Neotectonics of the Thakkhola graben and implications for recent activity on the South Tibetan fault system in the central Nepal Himalaya. *GSA Bull.* Retrieved from www.copyright.com

Jessup, M.J., Newell, D.L., Cottle, J.M., Berger, A.L. & Spotila, J.A. (2008) Orogen-parallel extension and exhumation enhanced by denudation in the trans-Himalayan Arun River gorge, Ama Drime Massif, Tibet-Nepal. *Geology*, **36**, 587–590. doi:10.1130/G24722A.1

Kellett, D.A., Grujic, D., Coutand, I., Cottle, J. & Mukul, M. (2013) The South Tibetan detachment system facilitates ultra rapid cooling of granulite-facies rocks in Sikkim Himalaya. *Tectonics*, **32**, 252–270. doi:10.1002/tect.20014

Kellett, D.A., Grujic, D. & Erdmann, S. (2009) Miocene structural reorganization of the South Tibetan detachment, eastern Himalaya: Implications for continental collision. *Lithosphere*, **1**, 259–281, Geological Society of America. doi:10.1130/L56.1

Kohn, M.J. (2008) P-T-t data from central Nepal support critical taper and repudiate large-scale channel flow of the Greater Himalayan Sequence. *GSA Bull.*, **120**, 259–273, GeoScienceWorld. doi:10.1130/B26252.1

Li, Y., Wang, C., Dai, J., Xu, G., Hou, Y. & Li, X. (2015) Propagation of the deformation and growth of the Tibetan-Himalayan orogen: A review. *Earth-Science Rev.* doi:10.1016/j.earscirev.2015.01.001

Liang, S., Gan, W., Shen, C., Xiao, G., Liu, J., Chen, W., Ding, X., *et al.* (2013) Three-dimensional velocity field of present-day crustal motion of the Tibetan Plateau derived from GPS measurements. *J. Geophys. Res. Solid Earth*. doi:10.1002/2013JB010503

Maiti, G. & Mandal, N. (2021) Early Miocene Exhumation of High-Pressure Rocks in the Himalaya: A Response to Reduced India-Asia Convergence Velocity. *Front. Earth Sci.* doi:10.3389/feart.2021.632806

Maiti, G., Mandal, N. & Misra, S. (2020) Insights into the dynamics of an orogenic wedge from lubrication theory: Implications for the Himalayan tectonics. *Tectonophysics*. doi:10.1016/j.tecto.2020.228335

Maiti, G., Roy, A., Sen, J. & Mandal, N. (2021) Impact of Decelerating India-Asia Convergence on the Crustal Flow Kinematics in Tibet: An Insight From Scaled Laboratory Modeling. *Geochemistry, Geophys. Geosystems*, **22**, e2021GC009967, John Wiley & Sons, Ltd. doi:10.1029/2021GC009967

McCaffrey, R. & Nabelek, J.L. (1998) Role of oblique convergence in the active deformation of the Himalayas and southern Tibet Plateau. *Geology*. doi:10.1130/0091-7613(1998)026<0691:ROOCIT>2.3.CO;2

Mitsuishi, M., Wallis, S.R., Aoya, M., Lee, J. & Wang, Y. (2012) E–W extension at 19 Ma in the Kung Co area, S. Tibet: Evidence for contemporaneous E–W and N–S extension in the Himalayan orogen. *Earth Planet. Sci. Lett.*, **325–326**, 10–20, Elsevier. doi:10.1016/J.EPSL.2011.11.013

Molnar, P. & Stock, J.M. (2009) Slowing of India's convergence with Eurasia since 20 Ma and its implications for Tibetan mantle dynamics. *Tectonics*. doi:10.1029/2008TC002271

Murphy, M.A., Yin, A., Kapp, P., Harrison, T.M., Manning, C.E., Ryerson, F.J., Lin, D., *et al.* (2002) Structural evolution of the Gurla Mandhata detachment system, southwest Tibet: Implications for the eastward extent of the Karakoram fault system. *GSA Bull.*, 428–447.

Pang, Y., Zhang, H., Gerya, T. V., Liao, J., Cheng, H. & Shi, Y. (2018) The Mechanism and Dynamics of N-S Rifting in Southern Tibet: Insight From 3-D Thermomechanical Modeling. *J. Geophys. Res. Solid Earth*. doi:10.1002/2017JB014011

Schellart, W.P., Chen, Z., Strak, V., Duarte, J.C. & Rosas, F.M. (2019) Pacific subduction control on Asian continental deformation including Tibetan extension and eastward extrusion tectonics. *Nat. Commun.* doi:10.1038/s41467-019-12337-9

Tapponnier, P., Peltzer, G., Dain, A.Y. Le, Armijo, R. & Cobbold, P. (1982) Propagating extrusion tectonics in Asia: new insights from simple experiments with plasticine. *Geology*. doi:10.1130/0091-7613(1982)10<611:PETIAN>2.0.CO;2

Wang, M. & Shen, Z.K. (2020) Present-Day Crustal Deformation of Continental China Derived From GPS and Its Tectonic Implications. *J. Geophys. Res. Solid Earth*, **125**, e2019JB018774, John Wiley & Sons, Ltd. doi:10.1029/2019JB018774

Yang, Y. & Liu, M. (2013) The indo-asian continental collision: A 3-D viscous model. *Tectonophysics*. doi:10.1016/j.tecto.2013.06.032

Zhang, P.Z., Shen, Z., Wang, M., Gan, W., Bürgmann, R., Molnar, P., Wang, Q., *et al.* (2004) Continuous deformation of the Tibetan Plateau from global positioning system data. *Geology*. doi:10.1130/G20554.1

Zheng, G., Wang, H., Wright, T.J., Lou, Y., Zhang, R., Zhang, W., Shi, C., *et al.* (2017) Crustal Deformation in the India-Eurasia Collision Zone From 25 Years of GPS Measurements. *J. Geophys. Res. Solid Earth*. doi:10.1002/2017JB014465

Zulauf, J. & Zulauf, G. (2004) Rheology of plasticine used as rock analogue: The impact of temperature, composition and strain. *J. Struct. Geol.* doi:10.1016/j.jsg.2003.07.005

Geophysical Research Letter
Supporting information for

N-S versus E-W extension in the Tibetan plateau: Are they driven by the same dynamics?

Giridas Maiti*[1], Arnab Roy[2], and Nibir Mandal[2]
[1] Institute of Applied Geosciences, Karlsruhe Institute for Technology, Germany
[2]Department of Geological Sciences, Jadavpur University, Kolkata, India

Contents of this file

S1. 2D Numerical experiments

Table S1
Parameters used in models

Mechanical and thermal parameters	**Units**	**Tibetan Upper &Mid crust**	**Tibetan Lower crust**	**Wedge**	**Lithospheric mantle**	**Mantle**
Thickness	km	45	25	To 100-130 km depth	35-130	To 410 km depth
Density (ρ)	kg m^{-3}	2800-2950	2950-3050	2600-3050	2900-3250	3250-3500
Effective viscosity (μ)	Pa s	10^{22}- 10^{21}	10^{21}	10^{21}-10^{20}	10^{22}-10^{21}	10^{20}-10^{19}
Heat capacity (C_p)	J $kg^{-1}K^{-1}$	750	750	750	1250	1250
Thermal conductivity (k)	W m^{-1} K^{-1}	2.25	2.25	2.25	2.25	2.25

Other mechanical parameters	**Units**	**Value**	**Other thermal parameters**	**Units**	**Value**
Model domain	km	1600 (horizontal)×410 (vertical)	Model surface temperature (T)	ºC	25
Convergence velocity of Indian plate (u)	cm/yr	2-10	T at bottom of lithospheric mantle (130 km)	ºC	1330
Upper boundary		Atmospheric pressure	Model bottom T (at 410 km depth)	ºC	1500
Left and right boundary of mantle domain		Free slip	Power law exponent (n)		-(1 to 3)
Basal boundary of mantle domain		Permeable	Viscosity co-efficient factor (μ_0)		10^{19}– 10^{23}
Right boundary of Asian lithosphere		No slip			

* Values of the mechanical and thermal parameters are taken from previous numerical studies on the Himalaya and other similar geodynamic setups [Warren et al., 2008; Li and Gerya, 2009; Flesch et al., 2001; Yang and Liu, 2013; Copley and Mckenzie, 2007]

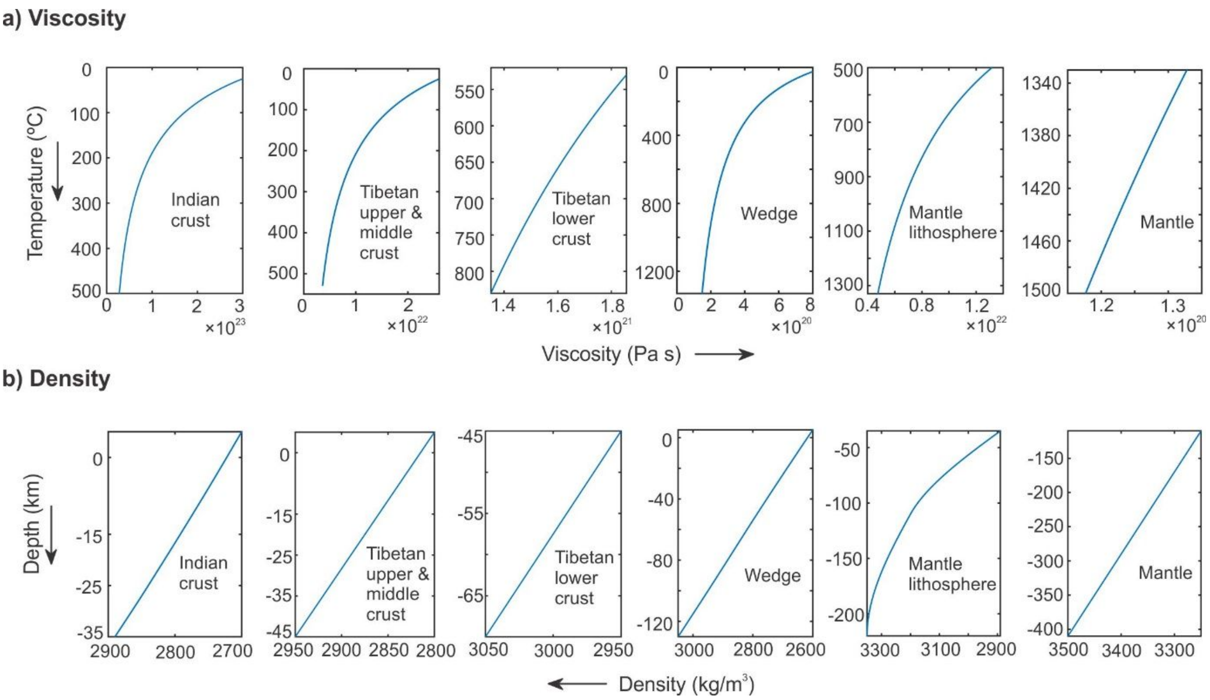

Figure S1: **a**) Calculated temperature dependent viscosities used for different model domains. Note that the effective viscosities of each unit agree with the bounds estimated by a number of previous studies in the Himalaya-Tibet system [Flesch et al., 2001; Yang and Liu, 2013; Copley and Mckenzie, 2007] **b**) Depth dependent densities for the model domains, constrained from geophysical estimates in the Himalaya-Tibet system, as summarized in Jimenez-Munt et al., 2008.

S2. Recording of 3D laboratory experiments

Characterization of velocity vectors in this study was executed using PIVlab, an image correlation algorithm written in Matlab. Cross correlation was performed on temporally successive image pairs which were captured with top view cameras. The correlation consisted of 2 passes with the 1st pass comprised of a preliminary 64 × 64 pixel interrogation zone for a coarse velocity calculation, followed by a 32 × 32 smaller interrogation zone for finer vector resolution. The velocity vectors were then exported in .vtk format in order to compute the strain rate tensors (Eq. S1) in Paraview.

$$\dot{\varepsilon}_{ij} = \frac{1}{2}\left(\frac{\partial u_i}{\partial x_j} + \frac{\partial u_j}{\partial x_i}\right) \quad \text{(S1)}$$

The Compute Derivatives tab in Paraview calculates the 9 component tensor (dU/dx, dU/dy, dU/dz, dV/dx, dV/dy, dV/dz, dW/dx, dW/dy, dV/dx, dW/dz) from the velocity vectors.

In this study, we made use of the multi-faceted and precise software MicMac (Galland et al. 2016; Rupnik et al. 2017) that applies photogrammetry in SfM algorithms to generate DEMs and 3D point clouds. The suitability of MicMac for laboratory models of geological processes has previously been tested by many workers. (Girod 2012; Galland et al. 2016). It is a free open-source software distributed under the CeCILL-B license. The main steps of the photogrammetric workflow in this study using MicMac are the following:

- Four photographs were simultaneously captured of the model from slightly different angles with the help of a 24.1 MP DSLR Nikon d5600 (Fig. S1). All images were analyzed with the photogrammetric software MicMac to compute tie points (Tapioca).
- The tie points were used to compute both the viewing angle and camera positions, and the distortion model of the cameras' optics (Tapas).
- The 3D transformation between the arbitrary system (Relative Orientation) and the georeferenced system was achieved with the help of ground control points (GCPBascule).
- A depth map was computed using all the images to create a 3D model through densification (Malt).
- A point cloud was generated (Nuage2Ply) which was further cleaned in Meshlab. The X, Y, Z coordinates of the point clouds were then plotted to create the topographic graphs.

For each time step of the model, we processed the four synchronous images taken by the four cameras with MicMac to produce a high-resolution DEM and an orthorectified image. The orthorectified images are advantageous as that they are very accurate depictions of the model surface because they have been corrected optical distortion of the lens and camera tilt. Thus, the orthorectified images can be used to measure distances and angles very accurately.

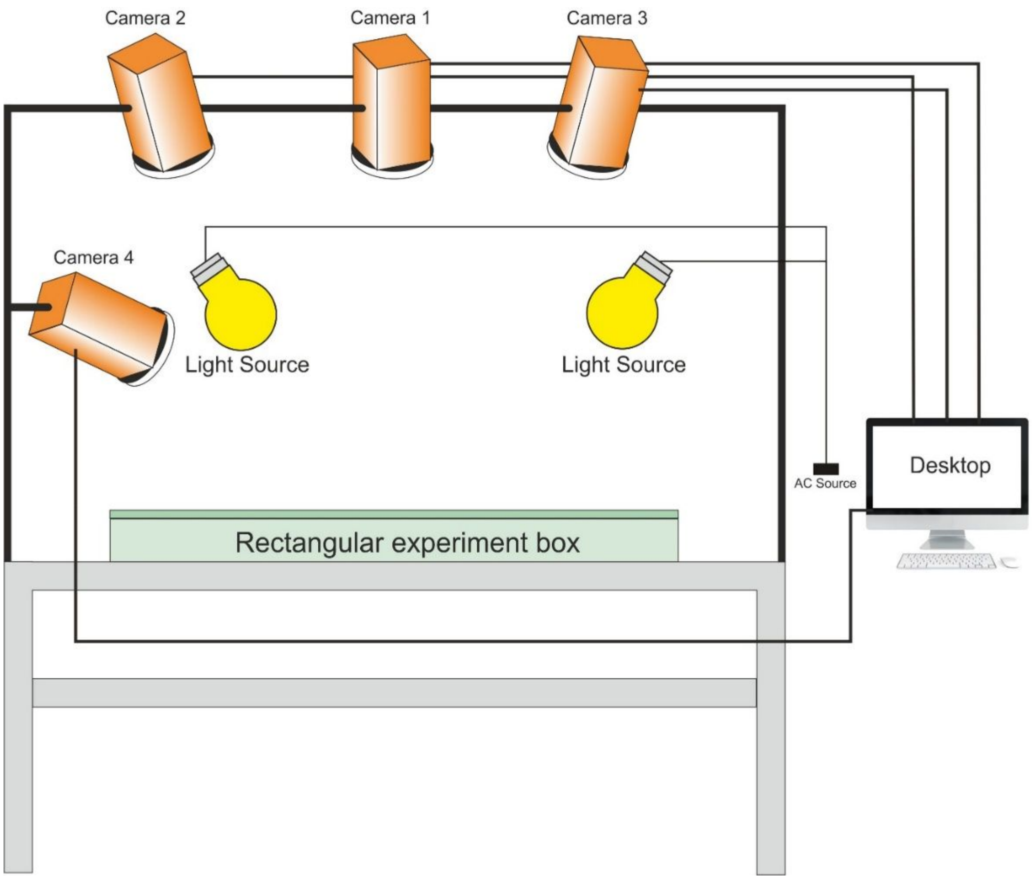

Figure S2: Experimental setup for PIV and topography analysis

Table S2. List of model parameters and their values chosen in laboratory experiments, along with their corresponding values for the natural prototypes (Liu & Yang 2003; Cook & Royden 2008; Schellart *et al.* 2019). The model scaling factors are provided in the extreme right column.

Parameters	**Model value (*m*)**	**Nature value (*n*)**	**Ratio (*m/n*)**
Gravity(g)	9.81 m/s^2	9.81 m/s^2	g_r =1
Length (l)	40 cm	3200 km	$l_r = 1.25\times10^{-7}$
Density (ρ)	1425 ± 3 kg/m^3	2950 kg/m^3	$\rho_r = 0.4831$
Viscosity (μ)	200 ± 5 Pa s	2×10^{21} Pa s	$\mu_r = 1\times10^{-19}$
Time ratio (t)	52.3 Seconds	1 Ma	$t_r = 1.6560\times10^{-12}$
Velocity (U)	U_m	U_n	$U_r = 7.5484\times10^4$

S3. 3D Numerical model setup and boundary conditions

We have constructed a three- dimensional (3D) mechanical model to show 3D nature of overriding Tibetan plateau's gravity collapse. The model domain has dimensions of 3450 × 2100 × 800 km in the *x*, *y* and *z* directions respectively. Material properties of each domain are same as in our 2D model. The top surface of Tibetan plateau approximates the topographic eastward topographic gradient measured at the time of gravitational collapse in the 3D laboratory model. In our model the Indian plate subducts at an angle 15° below the Eurasian plate. Tarim block and Sichuan basin surrounding the Tibetan plateau has been considered rigid and their position has been fixed based on plate reconstruction studies and earlier geodynamic models of India-Eurasia collision.